NJC

Accepted Manuscript

This is an *Accepted Manuscript*, which has been through the Royal Society of Chemistry peer review process and has been accepted for publication.

Accepted Manuscripts are published online shortly after acceptance, before technical editing, formatting and proof reading. Using this free service, authors can make their results available to the community, in citable form, before we publish the edited article. We will replace this *Accepted Manuscript* with the edited and formatted *Advance Article* as soon as it is available.

You can find more information about *Accepted Manuscripts* in the Information for Authors.

Please note that technical editing may introduce minor changes to the text and/or graphics, which may alter content. The journal's standard Terms & Conditions and the Ethical guidelines still apply. In no event shall the Royal Society of Chemistry be held responsible for any errors or omissions in this *Accepted Manuscript* or any consequences arising from the use of any information it contains.

ROYAL SOCIETY OF CHEMISTRY

www.rsc.org/njc

Design and synthesis of hierarchical $NiCo_2S_4$@$NiMoO_4$ core/shell nanospheres for high-performance supercapacitors

Mingming Yao, Zhonghua Hu*, Yafei Liu, Peipei Liu

The novel electrode material of three-dimensional (3D) hierarchical $NiCo_2S_4$@$NiMoO_4$ core/shell nanospheres for high-performance supercapacitors were successfully synthesized by a two-step method. First, ball-like $NiCo_2S_4$ was obtained by controlling the morphology through hydrothermal method by using diethanol amine as a new precipitant; second, the interconnected uniform $NiMoO_4$ nanosheets grew well on the backbone $NiCo_2S_4$ by hydrothermal method to form $NiCo_2S_4$@$NiMoO_4$ core/shell nanospheres. The resultant of hierarchical $NiCo_2S_4$@$NiMoO_4$ core/shell nanospheres were characterized by X-ray diffraction, energy dispersive spectrometer, X-ray photoelectron spectroscopy, field-emission scanning electron microscopy, transmission electron microscopy and N_2 adsorption and desorption. The electrochemical properties of the samples were evaluated though cyclic voltammetry, charge-discharge and electrochemical impedance spectroscopy in 6.0 M KOH electrolytic solution. The results showed that the hierarchical $NiCo_2S_4$@$NiMoO_4$ core/shell nanospheres exhibited a very large specific capacitance of 1714 F g^{-1} at 1 A g^{-1}, an outstanding cyclic stability with a capacitance retention of 96% after 5000 cycles of charge-discharge and a low resistance.

Introduction

Recently, development of advanced energy conversion and storage devices had been aroused worldwide interests to fulfill the surging energy demand in consumer mobile electronics and electric vehicles [1-4]. Supercapacitors, also called electrochemical capacitors, were recognized as important electrical energy storage devices due to its high specific power density, fast charge and discharge rate, long cycle life, safety and environmental friendliness [5-7]. The performances of supercapacitors depended mainly on the properties of their active electrode materials which could be usually divided into three types: carbon-based materials, conducting polymers and transition metal oxides. However, carbon-based material as one of the most widely used electrode materials had been badly hindered its further practical use for high-performance supercapacitors due to the fairly low specific and volumetric capacitances [8, 9]. Besides, conducting polymers exhibited poor stability during the charge-discharge cycling [10, 11]. Therefore, great efforts had been devoted to searching for inexpensive alternative transition metal oxides or their complexes with good capacitive characteristics, such as Co_3O_4, NiO and NiO/Co_3O_4 [12-14].

Among the various transition metal oxides electrode candidates, binary metal oxide/hydroxides were considered to be some of the most promising and low cost materials for high-performance specific capacitances because of their multiple oxidation states and structures that enabled multiple redox reactions, exhibiting higher performance than single component oxides/hydroxides [15-17]. $AMoO_4$ type materials had been attracted more research interest due to its potential application in electrical energy storage, $NiMoO_4$ as one of an attractive member, possessed a higher specific capacitance because of the high electrochemical activity of the nickel ion [18]. Yang et al. synthesized the Co_3O_4@$NiMoO_4$ nanosheets array through a facile chemical etching assistant approach, which could serve as a promising candidate for high-performance pseudocapacitive materials [19]. Hu et al. obtained the seaurchin-like $NiCo_2O_4$@$NiMoO_4$ nanomaterials, which exhibited the excellent electrochemical performance [20]. Additionally, considering for the lower optical band gap energy and much higher conductivity compared to $NiCo_2O_4$, $NiCo_2S_4$ had been raised great attention [21]. The replacement of oxygen with sulfur created

Department of Chemistry, Tongji University, 1239 Siping Road, Shanghai 200092, China

*Corresponding author. Tel.: +86 21 65982594; E-mail address: huzh@tongji.edu.cn. (Z. Hu)

more flexible structure due to its lower electronegativity than that of oxygen, prevent the disintegration of structure by the elongation between layers so that making it easy for electrons to transport in the structure, and enhance the electrochemical performances [22]. Dong and co-workers reported the $NiCo_2S_4$@MnO_2 heterostructure by a hydrothermal route, which exhibited an outstanding electrochemical performance due to the core-shell structure [23]. Therefore, the fabrication of metal oxide or binary metal oxide based composites with unique structures was an effective way to realize the high performance low-cost supercapacitors.

In this work, a novel 3D hierarchical $NiCo_2S_4$@$NiMoO_4$ core/shell nanospheres were designed and synthesized by a facile two-step hydrothermal method. The ball-like $NiCo_2S_4$ with rough surfaces obtained by controlling the morphology were the "core", whereas the interconnected uniform $NiMoO_4$ nanosheets were the "shell". To the best of our knowledge, the diethanol amine was a new precipitant to synthesis $NiCo_2S_4$ and the electrode of $NiCo_2S_4$@$NiMoO_4$ heterostructure with unique structure had not been reported before. Besides, this electrode material of 3D hierarchical $NiCo_2S_4$@$NiMoO_4$ core/shell nanospheres provided a high active surface area with hierarchical mesoporous structure but also had a strong synergistic effect from $NiCo_2S_4$ and $NiMoO_4$, showing attractive electrochemical behavior as electrode materials for pseudocapacitors.

Experimental

Material preparation

Nickel chloride hexahydrate ($NiCl_2{\cdot}6H_2O$), Cobalt chloride hexahydrate ($CoCl_2{\cdot}6H_2O$), sodiummolybdate dihydrate ($Na_2MoO_4{\cdot}2H_2O$), diethanol amine ($C_4H_{11}NO_2$), thiourea ($(H_4N)_2S$) and anhydrous ethanol (C_2H_6O) were purchased from Sinopharm Chemical Reagent Co. Ltd. Polytetrafluoroethylene (60%) was purchased from Shanghai 3F New Materials Co. Ltd. Nickel gauze was obtained from the Shanghai Hongxiang Plant. All the chemicals and reagents were of analytical grade and were used without further purification.

2 mmol of $NiCl_2{\cdot}6H_2O$ and 4 mmol of $CoCl_2{\cdot}6H_2O$ were dissolved in 40 mL of deionized water under magnetic stirring. Then, 12 mmol of thiourea was introduced into the Ni- and Co-containing solution slowly at room temperature with another continuous stirring for 30 min. Thereafter, added 40 mL of diethanol amine to above the mixed solution continually followed by a stirring for 20 min. The precursor was transferred to a Teflon-lined stainless steel autoclave and heated in an oven at 180°C for 16 h. After the autoclave cooled down to room temperature, the black precipitate was separated by filtration, washed with water and ethanol, dried at 100°C for 12 h to obtain the final product. In addition, the resultants of $NiCo_2S_4$ prepared at different hydrothermal time for controlling the morphology was studied.

To obtain hierarchical $NiCo_2S_4$@$NiMoO_4$ core/shell heterostructure, the subsequent hydrothermal growth of $NiMoO_4$ was processed in 80 mL aqueous solution containing 2.1 mmol of $NiCl_2{\cdot}6H_2O$ and 2.1 mmol $Na_2MoO_4{\cdot}2H_2O$. Then, 0.3 mmol $NiCo_2S_4$ was added into the above solution under the continuous stirring for 10 min, transferred the mixed solution to a Teflon-lined stainless steel autoclave, and heated to 120°C for 12h. After cooling down to room temperature, the products were taken out and rinsed with deionized water and alcohol several times, dried at 60°C for 12 h.

Characterization

Energy dispersive spectrometer (EDS) images were collected on an electron microscope, using a 200 kV accelerating voltage to identify $NiCo_2S_4$@$NiMoO_4$ heterostructure. X-ray photoelectron spectroscopy (XPS) was carried out by using ESCALAB 210 spectrometer (VG Scientific, UK). The crystal structure of prepared $NiCo_2S_4$@$NiMoO_4$ heterostructure was studied by X-ray diffraction (XRD, Bruker D8 Advance diffractometer) with Cu Kα (λ=0.15418 nm) radiation. The N_2 adsorption and desorption isotherms were measured by an automatic gas-adsorption apparatus (Micromeritics Tristar 3000) to estimate the porosity and surface area parameters. Brunauer-Emmett-Teller (BET) model and Barett-Joyner-Halenda (BJH) method were used to calculate the specific

surface areas and pore size distributions, respectively. The morphology of $NiCo_2S_4$@$NiMoO_4$ heterostructure was observed by field emission scanning electron microscopy (FESEM, XL30, Philips) and transmission electron microscopic (TEM, JEOL2100 microscope).

Electrochemical measurements

The working electrode containing 2-3 mg active materials (as-prepared $NiCo_2S_4$@$NiMoO_4$ heterostructure) were prepared by mixing the as-prepared $NiCo_2S_4$@$NiMoO_4$ heterostructure, graphite, and polytetrafluoroethylene in a mass ratio of 8 : 1 : 1 in a required amount of ethanol, and dried slightly at 60°C for 12 hours to form the paste. Then, the paste with a thickness of 1 mm, pressed by bead machine under 10 Mpa on Ni-gauze substrate and served as the working electrode which was soaked in 6 M KOH solution for 24 h to facilitate the electrolyte to completely diffuse into the pores of materials [24].

Cyclic voltammetry (CV) tests were performed in KOH electrolyte of 6 mol L^{-1} by using conventional three-electrode system (CHI600D, Shanghai Chenhua) at a scan rate of 5, 10, 20, 50 and 100 mV s^{-1} and in the potential window ranged from -0.4 to 0.55 V. The prepared $NiCo_2S_4$@$NiMoO_4$ electrode, nickel gauze and Ag/AgCl electrode were used as working, counter and reference electrodes, respectively.

The specific capacitance of the electrode materials is calculated from the charge-discharge curves according to the following Equation:

$$C_m = I\Delta t / \Delta V \cdot m \quad (1)$$

where C_m (F g^{-1}) is the specific capacitance, I (A) refers to the current density used for the charge-discharge measurements, Δt (s) refers to the time elapsed for the discharge cycle in the potential window, ΔV (V) represents the voltage interval of the discharge measurement and m (g) denotes the mass of active material in single electrode.

The electrochemical impedance spectra (EIS) were also recorded on the same electrochemical workstation. The frequency range is from 10 mHz to 1 MHz.

Moreover, the specific energy density E and power density P were calculated according to the following Equations:

$$E = 1/2\ C_m\ \Delta V^2 \quad (2)$$

$$P = E / \Delta t \quad (3)$$

where E is the specific energy density, C_m refers to the specific capacitance, ΔV is the voltage range, P represents the power density, and Δt is the discharge time.

Results and discussion

The purity and crystallinity of the $NiCo_2S_4$, $NiMoO_4$ and $NiCo_2S_4$@$NiMoO_4$ heterostructure were examined by wide-angel XRD pattern, as shown in Figure 1a. The five well-defined diffraction peaks appeared at 2θ values of 16.3, 26.8, 31.6 and 38.3, 55.3° could be indexed into the lattices of (111), (220), (311), (400) and (440) crystal planes of the $NiCo_2S_4$, respectively, corresponding to that of the standard pattern (JCPDS, No. 20-0782). No other diffraction peaks were detected, suggesting the high purity of the as-prepared $NiCo_2S_4$. In addition to the characteristic reflections from $NiCo_2S_4$, $NiMoO_4$ patterns were in good agreement with the standard patterns for $NiMoO_4 \cdot xH_2O$ (JCPDS, NO. 13-0128) and several diffraction peaks were attributed to the impurity phase of $NiMoO_4$ (JCPDS, NO. 12-0348), indicated the coexisting phases of $NiMoO_4$. The intensity diffraction peaks of $NiCo_2S_4$ in the $NiCo_2S_4$@$NiMoO_4$ pattern was reduced due to the covering of $NiMoO_4$ nanosheets on the surface of the $NiCo_2S_4$ nanomaterial. To confirm the formation of $NiCo_2S_4$@$NiMoO_4$ heterostructure, energy dispersive spectrometer analysis was also carried out, as shown in Figure 1b. It can clearly be seen that there are Ni, Co, Mo, S and O elements signals and no other signals were observed, it is further confirmed that the formation of $NiCo_2S_4$@$NiMoO_4$ heterostructure and agrees well with the results of XRD.

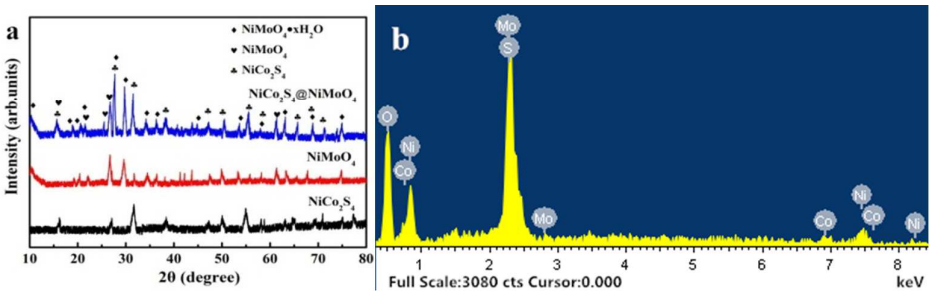

Figure 1. XRD pattern of the $NiCo_2S_4$, $NiMoO_4$ and $NiCo_2S_4$@ $NiMoO_4$ samples (a); EDS analysis of the $NiCo_2S_4$@$NiMoO_4$ heterostructure (b)

The elemental composition and chemical state of the porous $NiCo_2S_4$@$NiMoO_4$ heterostructure were characterized by X-ray photoelectron spectroscopy (XPS), as illustrated in Figure 2. Figure 2a indicated the presence of Ni, Co, Mo, S and O as well as C from the reference and no other elements were detected. According to a Gaussian fitting method, the Ni 2p spectrum (Figure 2b) could be well fitted with two spin-orbit doublets, which were the characteristics of Ni^{2+} and Ni^{3+}, and two shake-up satellites (identified as ''Sat.'') [25, 26]. The binding energy peaks were located at 858.1 eV and 876 eV, respectively, the main spin-energy separation of 17.9 eV, which was in accordance with Ni(II) oxidation state reported before [27]. Similar case to Co 2p spectrum (Figure 2c), the peak was fitted by spin-orbit characteristics of both Co^{2+} and Co^{3+}, and Co $2p_{3/2}$ and Co $2p_{1/2}$ peaks centered at 781.4 eV and 798.4 eV, respectively [28]. The strong peaks at 163.4 for S $2p_{1/2}$ and 162.2 eV for S $2p_{3/2}$ were demonstrated in Figure 2d, indicating the S element existing in $NiCo_2S_4$ [29]. The Mo 3d core level spectrum (Figure 2e) showed two peaks with binding energies of 233.9 eV and 236.9 eV corresponding to Mo $3d_{5/2}$ and Mo $3d_{3/2}$, respectively, and the binding energy peaks were also corresponding to a Mo(VI) oxidation state [30]. Figure 2f showed the spectrum of O 1s region, which was the typical metal-oxygen bonds located at 533.0 eV [31]. All these results showed that the surface of the as-prepared $NiCo_2S_4$@$NiMoO_4$ material with a composition containing Ni^{2+}, Ni^{3+}, Co^{2+}, Co^{3+}, S^{2-}, Mo^{6+} and O^{2-}, which was in good agreement with $NiCo_2S_4$ and $NiMoO_4$. Besides, the surface quantitative analysis based on XPS was also conducted. It showed that the surface automatic ratio of Ni/Mo/O was 1.22/1.03/4.31, which was close to the stoichiometric $NiMoO_4$ of 1/1/4. While the percentage of S was 2.46%, suggesting the main surface material was $NiMoO_4$ with only a few $NiCo_2S_4$ exposed. This result confirmed that the structure of $NiCo_2S_4$@$NiMoO_4$ nanomaterial, $NiCo_2S_4$ was the "core" and $NiMoO_4$ was the "shell".

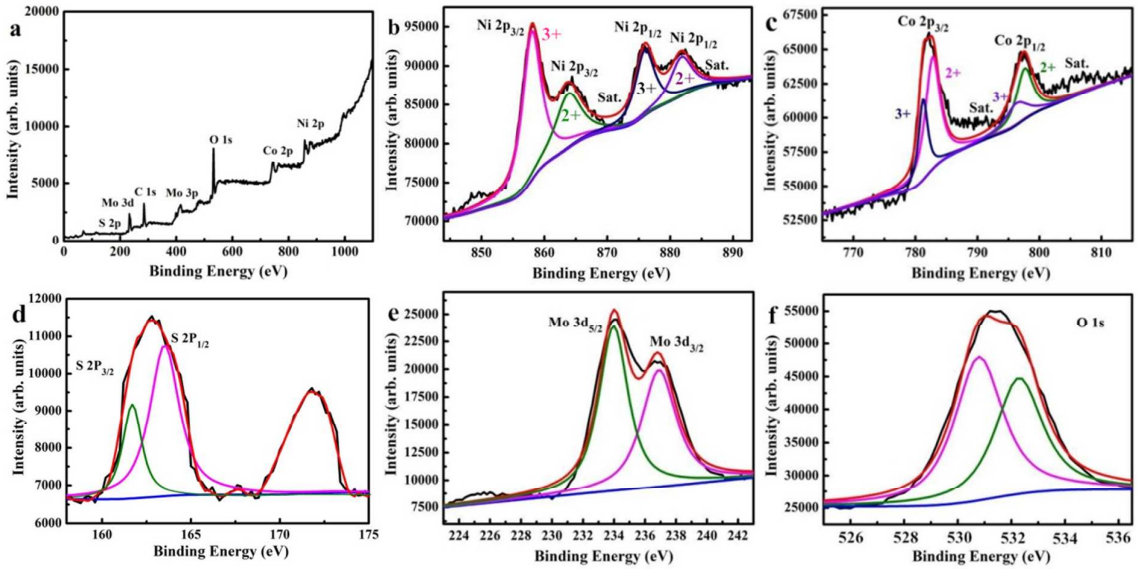

Figure 2. XPS spectra of survey spectrum (a), Ni 2p (b), Co 2p (c), S 2p (d), Mo 3d (e) and O 1s (f) for $NiCo_2S_4$@$NiMoO_4$ heterostructure

In order to investigate the most suitable morphology to become the "core" in the composites, the growing process of the $NiCo_2S_4$ shell was studied by inspecting the morphologies at different growth stages. Figure 3 showed the FESEM images for the products prepared with a reaction time of 8.0 and 12.0h. It was clearly that

acanthosphere-like particles were formed as the hydrothermal reaction time of 8.0h, as shown in Figure 3a. When the reaction time increased to 12.0h, the thorn was shortened and reduced (Figure 3b). As the reaction time prolonged to 16.0h, as shown in Figure 4a, the particles of $NiCo_2S_4$ become the ball-like shapes with rough surfaces, which was the most suitable morphology for the continuing grow of uniform $NiMoO_4$ nanosheets on it to form the $NiCo_2S_4$@$NiMoO_4$ heterostructure.

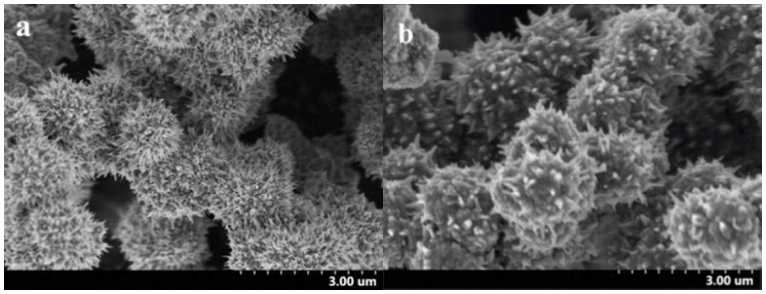

Figure 3. SEM images of the backbone $NiCo_2S_4$ prepared by hydrothermal method for 8 h (a) and 12 h (b)

The morphologies of $NiCo_2S_4$ and $NiCo_2S_4$@$NiMoO_4$ heterostructure were characterized by FESEM and the images were shown in Figure 4. The $NiCo_2S_4$ particles had the ball-like structure with rough surfaces, which also showed the diameter of 1.0-1.5 μm, as shown in Figure 4a and 4b. Figure 4c and 4d exhibited the morphology of $NiCo_2S_4$@$NiMoO_4$ core/shell heterostructure, it showed the nanospheres feature with the uniform nanosheets on the surface, so as to create a large amount of open-free space in the surface of nanospheres. It clearly displayed that the basic framework of $NiCo_2S_4$ ball was still retain well and uniformly wrapped by $NiMoO_4$ ultrathin nanosheets to form the $NiCo_2S_4$@$NiMoO_4$ core/shell nanospheres with the diameter about 2.0-2.5 μm.

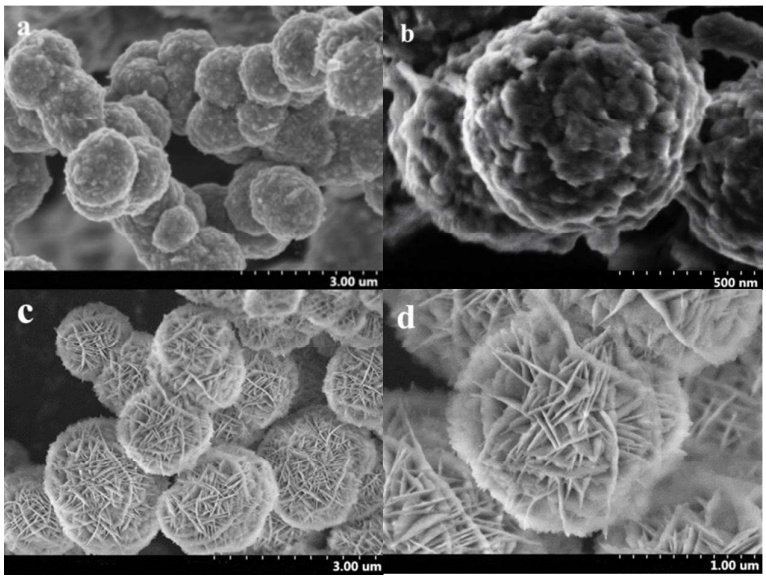

Figure 4. FESEM images of the backbone $NiCo_2S_4$ (a, b) and the $NiCo_2S_4$@$NiMoO_4$ heterostructure (c, d)

More details of the morphology and structure of the as-prepared $NiCo_2S_4$ and $NiCo_2S_4$@$NiMoO_4$ core/shell nanomaterials were characterized by using TEM and HRTEM. Figure 5a showed TEM image of the backbone structure of $NiCo_2S_4$ nanomaterial, It can clearly be seen that the quadrant with uneven surface; while Figure 5c showed the TEM image of the $NiCo_2S_4$@$NiMoO_4$ core/shell heterostructure for comparison, it indicated the well formation of nanosheets on the surface of $NiCo_2S_4$ as the sheet-like structure could be seen in the outlying and the morphology size was enlarged. The fringe spacing was estimated to be 0.279 nm and 0.165 nm according to the high-resolution TEM image shown in Figure 5b, and corresponded to the (311) and (440) planes of $NiCo_2S_4$ nanomaterial, respectively. In Figure 5d, it showed the clear lattice fringes of 0.263 nm and 0.281 nm, which was also in good agreement with that of XRD investigation.

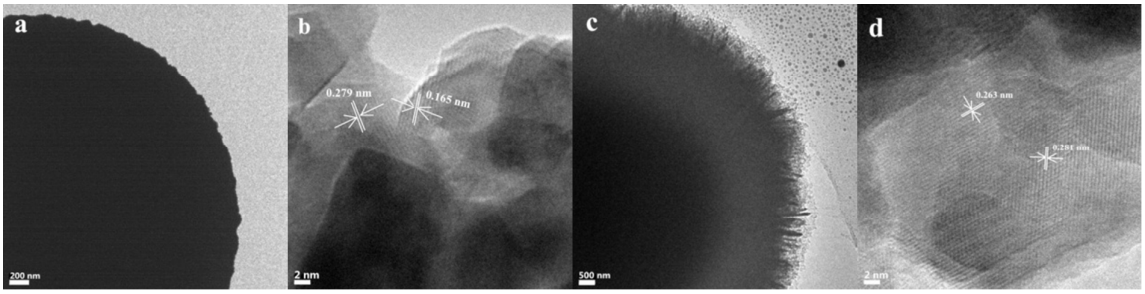

Figure 5. TEM image (a) and HRTEM image (b) of $NiCo_2S_4$; TEM image (c) and HRTEM image (d) of $NiCo_2S_4$@$NiMoO_4$ heterostructure

Figure 6 showed the N_2 adsorption/desorption isotherm and corresponding pore size distribution curve for the backbone of ball-like $NiCo_2S_4$, $NiMoO_4$ nanosheets and $NiCo_2S_4$@$NiMoO_4$ core/shell nanospheres. From Figure 6a, it could be seen that the pure ball-like $NiCo_2S_4$ exhibited the type-II curve with a low adsorption-desorption loop at the relative pressure P/P_0 of *ca*.0.6-1.0 [32], indicating an almost non-porous material with the surface area of 34 m^2g^{-1}; pure $NiMoO_4$ nanosheets had the combination of type-IV and -II isotherms with a small hysteresis loops, indicating the existence of a few mesoporous structures, and it showed the surface area of 45 m^2g^{-1}; while judged from the shape of the nitrogen adsorption isotherm of $NiCo_2S_4$@$NiMoO_4$ core/shell nanospheres, it essentially belonged to type-IV with the visible adsorbed-desorption loop at the relative pressure P/P_0 of *ca*.0.4-1.0, indicating the large amount of mesoporous structures reflected by the largest surface area of 95 m^2g^{-1}, which was larger than that previously reported for pure $NiCo_2S_4$ or pure $NiMoO_4$ nanomaterials [33, 34]. Moreover, the pore size distribution profile calculated from the adsorption branches of isotherms by using the BJH model was shown in figure 6b. The pore size distribution profile of $NiCo_2S_4$ exhibited the few mesopores with the pore size distribution of 5.2 nm and 7.3 nm; $NiMoO_4$ nanosheets displayed a narrow pore size distribution with a higher peak at 5.0 nm; while $NiCo_2S_4$@$NiMoO_4$ core/shell nanospheres contained dominant mesopores with the pore size distribution of 3.3 nm, 5.1 nm and 16.5 nm, indicating the evident characteristics of hierarchical mesoporous structure.

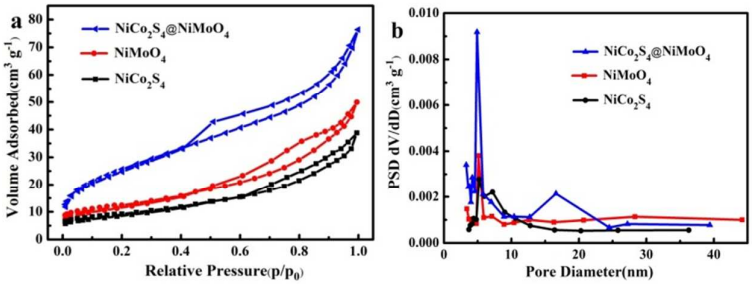

Figure 6. N_2 adsorption-desorption isotherm (a) and corresponding pore size distribution (b) of $NiCo_2S_4$, $NiMoO_4$ and $NiCo_2S_4$@$NiMoO_4$ core-shell heterostructure

On the basis of the above experimental descriptions and results, a formation mechanism of 3D hierarchical $NiCo_2S_4$@$NiMoO_4$ core/shell nanospheres involved two key steps, as illustrated in Figure 7. First, it was interest that the ball-like $NiCo_2S_4$ could be fabricated by adding the new precipitant of diethanol amine through the controllable of hydrothermal reaction time. In this experiment, diethanol amine as the weak alkali precipitant caused the slow reaction rate to facilitate the separation of nucleation and growth steps. Subsequently, a thin layer of uniform $NiMoO_4$ nanosheets interconnected together and coated onto the rough surface of the as-synthesized ball-like $NiCo_2S_4$, forming the hierarchical $NiCo_2S_4$@$NiMoO_4$ core/shell nanospheres successfully.

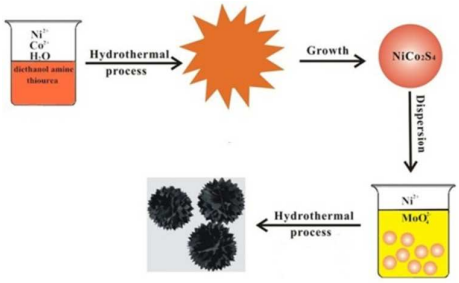

Figure 7. Schematic illustration of the synthesis process of hierarchical $NiCo_2S_4$@$NiMoO_4$ core-shell nanospheres

The pseudocapacitive properties of hierarchical $NiCo_2S_4$@$NiMoO_4$ core/shell nanospheres were investigated for their potential application in electrochemical energy storage. Figure 8a showed the CV curves of the bare $NiCo_2S_4$ core, $NiMoO_4$ shell and $NiCo_2S_4$@$NiMoO_4$ heterostructure electrode at a scan rate of 10 mV s^{-1}. Figure 8b showed the charge-discharge curves of the bare $NiCo_2S_4$ core, $NiMoO_4$ shell and $NiCo_2S_4$@$NiMoO_4$ heterostructure electrode at a current density of 1 A g^{-1} in 6 M KOH electrolyte in the voltage range of 0.0-0.35 V. In Figure 8a, Well-defined redox peaks were observed for these nanomaterials indicating the capacitance mainly results from the contribution of faradaic pseudo-capacitance. The prominent redox peaks observed in the CV curve of $NiCo_2S_4$ was due to the reversible redox reactions of Ni^{2+}/Ni^{3+}, $Co^{2+}/Co^{3+}$and Co^{3+}/Co^{4+} transitions based on the following equations [23, 35]:

$$CoS + OH^- \leftrightarrow CoSOH + e^- \quad (4)$$

$$CoSOH + OH^- \leftrightarrow CoSO + H_2O + e^- \quad (5)$$

$$NiS + OH^- \leftrightarrow NiSOH + e^- \quad (6)$$

The CV curve of $NiMoO_4$ also consisted of a pair of strong redox peaks which originated from faradaic reactions as follows [36]

$$Ni(II) \leftrightarrow Ni(III) + e^- \quad (7)$$

While $NiCo_2S_4$@$NiMoO_4$ CV curve almost contained both $NiCo_2S_4$ and $NiMoO_4$ redox peaks, and the integral CV area was larger than the pure $NiCo_2S_4$ and $NiMoO_4$, indicating that the $NiCo_2S_4$@$NiMoO_4$ electrode had a largest specific capacitance at the same scan rate, which also could have been proved by charge-discharge curves in Figure 8b. It was mainly owing to the core-shell nanospheres with the hierarchical structure and large specific surface area to create more electrochemical reaction activities. Moreover, the open and free interspaces both among these interconnected nanosheets and inside ball with the rough surfaces could act as an "ion reservoir" that could shorten the diffusion distance from the external electrolyte to the interior surfaces and then minimized ion transport resistance, thus enhanced the electrochemical performances [37].

Figure 8c showed the CV curves of the $NiCo_2S_4$@$NiMoO_4$ electrodes in 6 M KOH electrolyte in a potential range of -0.4-0.55 V. From the curves, it could be seen that the anodic peaks shifted towards positive potential and the cathodic peaks shifted towards negative potential, which may be attributed to the increasing electric polarization and irreversible reactions as the scan rate scales up [38]. Besides, well defined redox peaks were kept in all CV curves which contributed from faradaic redox. Since the redox reactions usually depended on the intercalation-deintercalation of protons from the electrolyte, at lower scan rates, the diffusion of ions from the electrolyte can enter into almost all the effective holes of the electrode [39]. While as the scan rate increased, the effective interaction between the ions and the electrode was greatly reduced, which leads to a lower areal capacitance [40].

Figure 8d displayed the charge-discharge curves of $NiCo_2S_4$@$NiMoO_4$ electrode at the current density from 1 to 20 A g^{-1} in 6 M KOH electrolyte in the voltage range of 0.0-0.35 V (vs. Ag/AgCl). The $NiCo_2S_4$@$NiMoO_4$ electrode possessed the pseudocapacitive behavior of metallic oxides with the small potential drop at low current densities, implying a small internal resistance of the electrode material. According to the equation (1), the specific capacitance was calculated to be 1714 F g^{-1} at the current density of 1 A g^{-1}, much higher than the pure $NiCo_2S_4$ (1030 F g^{-1} at 1 A g^{-1}) and $NiMoO_4$ (1206 F g^{-1} at 1 A g^{-1}) electrode, which was due to the synergistic effects in heterostructured materials with the superior electrochemical performance [41]. As the current density increased from 1 to 20 A g^{-1} (Figure 8e), the specific capacitance of $NiCo_2S_4$@$NiMoO_4$ electrode decreased to 1314 F g^{-1}, it was probably due to the incremental voltage drop and the insufficient active material involved in the redox reaction. The massive OH^- ions were required to intercalate swiftly at the interface of the electrode/electrolyte when the electrode at the high sweep rates, however, the OH^- ions could not meet this demand, this was the process of ionic diffusion controlled [42]. However, $NiCo_2S_4$@$NiMoO_4$ electrode exhibited the superior capacitance retention, 23% specific capacitance decreased when the current density increases by 20 times and still higher than the pure $NiCo_2S_4$ and $NiMoO_4$ nanomaterials.

To further understand the electrochemical performances and characteristics of $NiCo_2S_4$@$NiMoO_4$ electrode, the electrochemical impedance spectroscopy (EIS) was carried out. EIS analysis of pure $NiCo_2S_4$, $NiMoO_4$ electrode and $NiCo_2S_4$@$NiMoO_4$ electrode were measured and the corresponding Nyquist plots were shown in Figure 8f, it could be seen that the EIS data consists of three parts: first, Warburg resistance reflected from the slope of the EIS curve in the low frequency range, which described the diffusion of redox species in the electrolyte; second, charge transfer resistance (*Rct*), which the numerical value equal to the diameter of the semicircle on the Z_{real} axis in the high frequency range and results from the diffusion of electrons [43]; third, internal resistance (R_e), which was the intercept on the real axis in the high frequency range includes the inherent resistances of the electroactive material, bulk resistance of electrolyte, and contact resistance at the interface between electrolyte and electrode [44]. Therefore, it could be observed in Figure 8f that the $NiCo_2S_4$@$NiMoO_4$ electrode had the resistances

of 0.62Ω, which was lower than the $NiMoO_4$ shell (0.84Ω), suggesting that the introduction of $NiCo_2S_4$ core improved the electron conductivity of $NiCo_2S_4$@$NiMoO_4$ electrode.

The cycling stability was also evaluated by the repeated charging-discharging measurements at a high discharge current density of 10 A g^{-1} for 5000 cycles, as shown in Figure 8g. Remarkably, 96% capacitance was still retained after 5000 cycles, which was remarkably higher than the pure $NiCo_2S_4$ (90%) and $NiMoO_4$ (93%) electrode. Therefore, the cycling stability of the hierarchical $NiCo_2S_4$@$NiMoO_4$ core/shell nanospheres at high current density was further improved, it may be due to the interconnected $NiMoO_4$ nanosheets covered on the surface of $NiCo_2S_4$ core created more diffusion paths, significantly enhance the intercalation/deintercalation of ions and improve the utilization rate of electrode materials even at high rates [21].

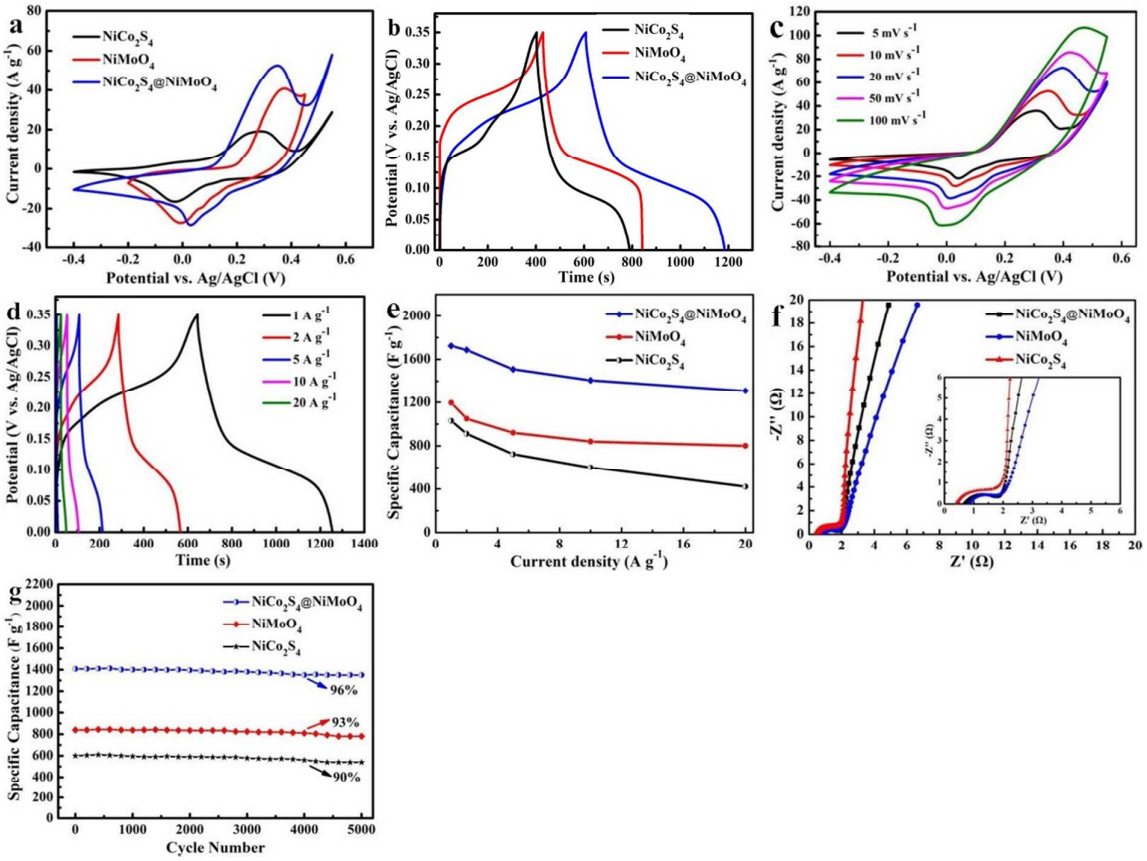

Figure 8. Electrochemical performances of $NiCo_2S_4$, $NiMoO_4$ and $NiCo_2S_4$@$NiMoO_4$ electrodes: comparative CV curves recorded at a scan rate of 10 mV s^{-1} for the three different electrodes (a); comparative charge-discharge curves at a current density of 1 A g^{-1} for the three different electrodes (b); CV curves at different scan rates for $NiCo_2S_4$@$NiMoO_4$ electrode (c); charge-discharge curves at different current densities of $NiCo_2S_4$@$NiMoO_4$ electrode (d); AC impedance plots of three electrodes (e); specific capacitance as a function of discharge current density (f); variation of specific capacitance with cycle numbers at a current density of 10 A g^{-1} (g)

In order to further demonstrate the potential application of hierarchical $NiCo_2S_4$@$NiMoO_4$ core/shell nanospheres in supercapacitors, the Ragone plots for $NiCo_2S_4$@$NiMoO_4$ electrode was displayed to show the relation between energy and power density, as shown in Figure 9. $NiCo_2S_4$@$NiMoO_4$ electrode delivered a high energy density of 29.1 Wh kg^{-1} at a power density of 172 W kg^{-1}, and had a little sacrifice of 7 Wh kg^{-1} as power outputs range increased to 3340 W kg^{-1}. Additionally, the pure $NiCo_2S_4$ and $NiMoO_4$ electrode exhibited slightly reduced but still quite good energy densities with the similar power densities. These obtainable results made the present hierarchical $NiCo_2S_4$@$NiMoO_4$ core/shell nanospheres were the appealing electrode materials for advanced supercapacitors.

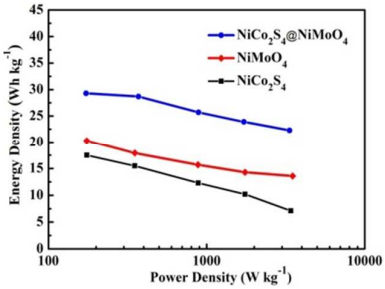

Figure 9. Ragone plot of the estimated specific energy and specific power at various charge-discharge rates

Table 1 showed the specific capacitance of $NiCo_2S_4$@$NiMoO_4$ electrode prepared in the present work and other heterostructured materials from literatures for the comparison, given more clearly clarification of the good electrochemical performances of hierarchical $NiCo_2S_4$@$NiMoO_4$ core/shell nanospheres, which prepared by using a new precipitant of diethanol amine through the facile two-step hydrothermal method. The results demonstrated that this 3D hierarchical $NiCo_2S_4$@$NiMoO_4$ core/shell nanomaterial had the novel morphology of nanospheres, it possessed a large specific capacitance and suitable pore size distribution. The large specific surface area could beneficial for the electrolyte ions diffusion to the active material and effectively improve the pseudocapacitance of electrode; besides, the hierarchical mesopores with the pore size distribution of 2-5 nm could provide rich electroactive sites and short diffusion paths for charge transports, which were required in the Faradaic redox reactions [47]; impressively, the interconnected $NiMoO_4$ nanosheets shell combined the not fully covered $NiCo_2S_4$ core with the rough surface made the effective diffusion of electrolyte participate in the electrochemical charge storage, which realized a strong synergistic effect to enhance the pseudocapacitance behavior. The three aspects referred above contribute to the superior electrochemical properties of as-prepared hierarchical $NiCo_2S_4$@$NiMoO_4$ core/shell nanospheres.

Table 1 Comparison of the specific capacitance of $NiCo_2S_4$@$NiMoO_4$ electrode prepared in present work and that published in the literatures

Sample	C_m (F g^{-1})	Ref.
$NiCo_2S_4$@$NiMoO_4$ nanospheres	1597 (2 A g^{-1})	this work
$NiCo_2S_4$@MnO_2 heterostructures	1337.8 (2 A g^{-1})	[23]
$CoMoO_4$-$NiMoO_4 \cdot xH_2O$ bundles	1039 (2.5 mA cm^{-2})	[18]
Co_3O_4@$NiMoO_4$ nanosheets	1526 (3 mA cm^{-2})	[19]
Co_3O_4@$NiMoO_4$ nanowires	1230 (10 mA cm^{-2})	[45]
$NiCo_2O_4$@$NiCo_2O_4$ nanoflake	1115.6 (5 mA cm^{-2})	[46]

Conclusions

A facile and cost-effective two-step hydrothermal approach to synthesized the unique hierarchical $NiCo_2S_4$@$NiMoO_4$ core/shell nanospheres was proposed. The ball-like $NiCo_2S_4$ nanostructure was obtained by controlling the morphology using diethanol amine as a new precipitant. Then the interconnected uniform $NiMoO_4$ nanosheets grew well on the backbone $NiCo_2S_4$ to form $NiCo_2S_4$@$NiMoO_4$ core/shell nanospheres. The results demonstrated that the as-synthesized hierarchical $NiCo_2S_4$@$NiMoO_4$ core/shell nanospheres with the large specific surface area had superior specific capacitance of 1714 F g^{-1} under 1.0 A g^{-1}; it exhibited a good cycling stability and conductivity. All the outstanding performances highlight the potential of using binary metal oxide based electrode for widespread supercapacitor applications.

Acknowledgments

This work was supported by Tongji University Research Foundation (1380219039). The authors would like to thank the workers from the Chemistry Experimentation Center of Tongji University and laboratory members for their help.

Notes and References

[1] P. Simon and Y. Gogotsi, *Nat. Mater.*, 2008, **7**, 845.

[2] N. S. Choi, Z. H. Chen, S. A. Freunberger, X. L. Ji, Y. K. Sun, K. Amine, G. Yushin, L. F. Nazar, J. Cho and P. G. Bruce, *Angew. Chem., Int. Ed.*, 2012, **51**, 9994.
[3] J. Jiang, Y. Y. Li, J. P. Liu, X. T. Huang, C. Z. Yuan and X. W. Lou, *Adv. Mater.*, 2012, **24**, 5166.
[4] M. X. Liu, L. H. Gan, W. Xiong, F. Q. Zhao, X. Z. Fan, D. Z. Zhu, Z. J. Xu, Z. X. Hao and L. W. Chen, *Energy Fuels*, 2013, **27**, 1168.
[5] G. Wang, L. Zhang and J. Zhang, *Chem. Soc. Rev.*, 2012, **41**, 797.
[6] M. M. Yao, Z. H. Hu, Z. J. Xu, Y. F. Liu, P. P. Liu and Q. Zhang, *J. Power Sources*, 2015, **273**, 914.
[7] M. X. Liu, L. H. Gan, W. Xiong, Z. J. Xu, D. Z. Zhu and L. W. Chen, *J. Mater. Chem. A*, 2014, **2**, 2555.
[8] Y. Huang, J. Liang and Y. Chen, *Small*, 2012, **8**, 1805.
[9] R. L. McCreery, *Chem. Rev.*, 2008, **108**, 2646.
[10] S. J. Ding, T. Zhu, J. S. Chen, Z, Y. Wang, C. L. Yuan and X. W. Lou, *J. Mater. Chem.*, 2011, **21**, 6602.
[11] H. L. Wang, H. S. Casalongue, Y. Y. Liang and H. J. Dai, *J. Am. Chem. Soc.*, 2010, **132**, 7472.
[12] Y. Y. Wang, Y. Lei, J. Li, L. Gu, H. Y. Yuan and D. Xiao, *ACS Appl. Mater. Interfaces*, 2014, **6**, 6739.
[13] M. M. Yao, Z. H. Hu, Z. J. Xu, Y. F. Liu, P. P. Liu and Q. Zhang, *Electrochim. Acta*, 2015, **158**, 96.
[14] K. B. Xu, R. J. Zou, W. Y. Li, Y. F. Xue, G. S. Song, Q. Liu, X. J. Liu and J. Q. Hu, *J. Mater. Chem. A*, 2013, **1**, 9107.
[15] H. Jiang, J. Ma and C. Z. Li, *Chem. Commun.*, 2012, **48**, 4465.
[16] T. Y. Wei, C. H. Chen, H. C. Chien, S. Y. Lu and C. C. Hu, *Adv. Mater.*, 2010, **22**, 347.
[17] M. C. Liu, L. B. Kong, X. J. Ma, C. Lu, X. M. Li, Y. C. Luo and L. Kang, *New J. Chem.*, 2012, **36**, 1713.
[18] M. C. Liu, L. B. Kong, C. Lu, X. J. Ma, X. M. Li, Y. C. Luo and L. Kang, *J. Mater. Chem. A*, 2013, **1**, 1380.
[19] W. Hong, J. Q. Wang, P. W. Gong, J. F. Sun, L. Y. Niu, Z. G. Yang, Z. F. Wang and S. R. Yang, *J. Power Sources*, 2014, **270**, 516.
[20] Q. Zhang, Y. H. Deng, Z. H. Hu, Y. F. Liu, M. M. Yao and P. P. Liu, *Phys. Chem. Chem. Phys.*, 2014, **16**, 23451.
[21] H. Chen, J. Jiang, L. Zhang, H. Wan, T. Qi and D. Xia, *Nanoscale*, 2013, **5**, 8879.
[22] S. H. Park, Y. K. Sun, K. S. Park, K. S. Nahm, Y. S. Lee and M. Yoshio, *Electrochim. Acta*, 2002, **47**, 1721.
[23] J. Yang, M. Z. Ma, C. C. Sun, Y. F. Zhang, W. Huang and X. C. Dong, *J. Mater. Chem. A*, 2015, **3**, 1258.
[24] Y. H. Zhao, M. X. Liu, L. H. Gan, X. M. Ma, D. Z. Zhu, Z. J. Xu and L. W. Chen, *Energy Fuels*, 2014, **28**, 1561.
[25] Y. Meng, K. Wang, Y. Zhang and Z. Wei, *Adv. Mater.*, 2013, **25**, 6985.
[26] Y. Liu, J. N. Zhang, S. P. Wang, K. X. Wang, Z. M. Chen and Q. Xu, *New J. Chem.*, 2014, **38**, 4045.
[27] J. Yan, Z. J. Fan, W. Sun, G. Q. Ning, T. Wei, Q. Zhang, R. F. Zhang, L. J. Zhi and F. Wei, *Adv. Funct. Mater.*, 2012, **22**, 2632.
[28] J. Pu, F. L. Cui, S. B. Chu, T. G. Wang, E. H. Sheng and Z. H. Wang, *ACS Sustain. Chem. Eng.*, 2014, **2**, 809.
[29] Q. H. Wang, L. F. Jiao, H. M. Du, Y. C. Si, Y. J. Wang and H. T. Yuan, *J. Mater. Chem.*, 2012, **22**, 21387.
[30] X. Xia, W. Lei, Q. Hao, W. Wang and X. Wang, *Electrochim. Acta*, 2013, **99**, 253.
[31] Y. E. Roginskaya, Q. Morozova, E. Lubnin, Y. E. Ulitina, G. Lopukhova and S. Trasatti, *Langmuir*, 1997, **13**, 4621.
[32] T. Siemieniewska, K. S. Sing, J. Rouquerol, R. A. Pierotti, L. Moscou, R. A. Haul and D. H. Evereit, *Pure Appl. Chem.*, 1985, **57**, 603.
[33] Y. R. Zhu, Z. B. Wu, M. J. Jing, X. M. Yang, W. X. Song and X. B. Ji, *J. Power Sources*, 2015, **273**, 584.
[34] D. P. Cai, D. D. Wang, B. Liu, Y. R. Wang, Y. Liu, L. L. Wang, H. Li, H. Huang, Q. H. Li and T. H. Wang, *ACS Appl. Mater. Interfaces*, 2013, **5**, 12905.
[35] J. Xiao, L. Wan, S. Yang, F. Xiao and S. Wang, *Nano Lett.*, 2014, 14, 831.
[36] B. Senthilkumar, S. Vijaya, K. S. Kalimuthu, M. Ramakrishnan and M. M. Danielle, *RSC Adv.*, 2013, **3**, 352.
[37] D. W. Wang, F. Li, M. Liu, G. Q. Lu and H. M. Cheng, *Angew. Chem. Int. Ed.*, 2008, **47**, 373.
[38] L. Fan, L. Tang, H. F. Gong, Z. H. Yao and R. Guo, *J. Mater. Chem.*, 2012, **22**, 16376.
[39] Q. F. Wang, B. Liu, X. F. Wang, S. H. Ran, L. M. Wang, D. Chen and G. Z. Shen, J. Mater. Chem., 2012, **22,** 21647.
[40] L. Mei, T. Yang, C. Xu, M. Zhang, L. B. Chen, Q. H. Li and T. H. Wang, *Nano Energy*, 2014, **3**, 36.
[41] L. Q. Mai, F. Yang, Y. L. Zhao, X. Xu, L. Xu and Y. Z. Luo, *Nat. Commun.*, 2011, **2**, 1387/1.
[42] K. B. Hatzell, M. Beidaghi, J. W. Campos, C. R. Dennison, E. C. Kumbur and Y. Gogotsi, *Electrochim. Acta*, 2013, **111**, 888.
[43] K. X. Li, Y. H. Luo, Z. X. Yu, M. H. Deng, D. M. Li and Q. B. Meng, *Electrochem. Commun.*, 2009, **11**, 1346.
[44] C. Z. Yuan, X. G. Zhang, Q. F. Wu and B. Gao, *Solid State Ionics*, 2006, **177**, 1237.
[45] D. P. Cai, D. D. Wang, B. Liu, L. L. Wang, Y. Liu, H. Li, Y. R. Wang, Q. H. Li and T. H. Wang, *ACS Appl. Mater. Interfaces*, 2014, **6**, 5050.
[46] X. Y. Liu, S. J. Shi, Q. Q. Xiong, L. Li, Y. J. Zhang, H. Tang, C. D. Gu, X. L. Wang and J. P. Tu, *ACS Appl. Mater. Interfaces*, 2013, **5**, 8790.
[47] L. Shen, H. Che, H. Li and X. Zhang, *Adv. Funct. Mater.*, 2014, **24**, 2630.

Graphical Abstract

The novel electrode material of three-dimensional hierarchical $NiCo_2S_4$@$NiMoO_4$ core/shell nanospheres were synthesized by a facile two-step hydrothermal method. This hierarchical $NiCo_2S_4$@$NiMoO_4$ core/shell nanospheres exhibit the high specific capacitance of 1714 F g^{-1} at the current density of 1 A g^{-1} which indicated the excellent electrochemistry performance.